

# Agile Underwater Swimming of Magnetic Polymeric Microrobots in Viscous Solutions

Sukyoung Won, Hyeongmin Je, Sanha Kim,\* and Jeong Jae Wie\*

Miniaturization of polymeric robots leads to difficulties in actuation inside viscous media due to the increased surface drag on the diminutive robot bodies. Herein, agile underwater swimming of polymeric microrobots is presented with the investigation of correlation between the magnetic propulsion and viscous drag on the robot. The polymeric microrobots swim with pivoting and tumbling motions during underwater rotation by in-plane rotation of two permanent magnets underneath the plane, which results in orbital revolution-type locomotion with a maximum swimming velocity of 56 body lengths per second ( $\text{BL s}^{-1}$ ). The rotational ability and orbital velocity of the polymeric microrobots are determined by correlated variables, i.e., liquid viscosity and frequency of magnet rotation, as elucidated by experimental results and theoretical analysis. Based on the understanding of underwater orbital maneuvers, the polymeric microrobots achieve agile swimmability at a viscosity similar to that of normal whole blood and self-correcting maneuverability in diverse vascular-like environments, including a stenosed tube with a coarse granular hill and a rough-walled artificial blood vessel. Agile underwater swimming can improve versatile aquatic performances of miniaturized robots in blood vessels with arteriosclerosis or blood clots.

## 1. Introduction

Polymer-based robotic devices have been developed into diverse 3D structures via deformability of polymers during polymerization, as well as thermal processing above glass transition temperature, nematic-to-isotropic transition, or melting temperature.<sup>[1–3]</sup> In miniaturized robotics, lights<sup>[4–7]</sup> and magnetic fields<sup>[8–10]</sup> have emerged as promising stimuli for contactless manipulation of the polymeric robotic matters. Remote powered systems are advantageous in that they avoid the weight penalty of onboard batteries and wire components. The miniaturized polymeric robots are manipulated through shape morphing of local position in the robots or rotational or translational motion of the whole bodies.<sup>[11]</sup> Photo-triggered actuation is driven by local shape morphing of photoisomerized liquid crystalline polymers<sup>[12,13]</sup> and local volumetric changes in hydrogels.<sup>[14]</sup> Spatiotemporal control of light further allows on-demand shape

morphing of photoactive liquid crystalline polymers.<sup>[15]</sup> However, photoinduced actuation is governed by Beer–Lambert law, which limits the penetration depth of the light field along the propagation pathway. Photomotility of the miniaturized robots eventually disappears when opaque barriers prohibit the transmittance of actinic light, hindering in vivo operation of the miniaturized robots.

In contrast, miniaturized magnetic polymeric robots are more effective at navigating in enclosed environments owing to the penetrating force of magnetic fields, making them of particular interest in the field of biomechanical engineering.<sup>[16]</sup> Miniaturized magnetic polymeric robots are propelled by the gradient of the magnetic field,<sup>[17,18]</sup> the magnetic torque,<sup>[19,20]</sup> or a combination of both.<sup>[21,22]</sup> Gradient-driven mechanism utilizes nonuniform magnetic force, whereas magnetic torque is based on the time-varying, space-uniform magnetic field. Most micrometer-scale magnetic polymeric robots are actuated by manipulating rotating magnetic fields of uniform intensities. The microrobots are designed to be helical polymer structures of double-helices, spring, or flagella-mimetics<sup>[23–25]</sup> for swimming capability. When multiaxial electromagnetic coils generate rotating magnetic fields, the helical polymeric microrobots demonstrate translational corkscrew motions.

Magnetomotility of the helical microrobots can be driven by the magnetic torque generated when the direction of the

S. Won, J. J. Wie  
Department of Polymer Science and Engineering  
Inha University  
100 Inha-ro, Michuhol-gu, Incheon 22212, Republic of Korea  
E-mail: wie@inha.ac.kr

S. Won, J. J. Wie  
Program in Environmental and Polymer Engineering  
Inha University  
100 Inha-ro, Michuhol-gu, Incheon 22212, Republic of Korea

H. Je, S. Kim  
Department of Mechanical Engineering  
Korea Advanced Institute of Science and Technology  
291 Daehak-ro, Yuseong-gu, Daejeon 34141, Republic of Korea  
E-mail: sanhkim@kaist.ac.kr

 The ORCID identification number(s) for the author(s) of this article can be found under <https://doi.org/10.1002/aisy.202100269>.

© 2022 The Authors. Advanced Intelligent Systems published by Wiley-VCH GmbH. This is an open access article under the terms of the Creative Commons Attribution License, which permits use, distribution and reproduction in any medium, provided the original work is properly cited.

DOI: 10.1002/aisy.202100269

magnetic dipole moments inside the robot is mismatched with the direction of the external magnetic fields. To improve swimming velocity of helical-structure microrobots in viscous media, experimental and theoretical modeling have been investigated for microrobots manipulation via rotating electromagnetic fields.<sup>[25,26]</sup> However, enhancement of swimming velocity is needed to ensure effective swimming of helical polymeric microrobots in viscous media of vascular endothelium. Although the swimming capability of magnetic microrobots is intrinsically essential for biomedical functionalities<sup>[27,28]</sup> such as anticoagulation and medical imaging, magnetic polymeric microrobots have thus far only demonstrated swimming velocities of a few micrometers per second ( $<10 \text{ BL s}^{-1}$ ). Swimming velocity of polymeric microrobots can be improved by programming robot geometry during polymerization or in thermal processing. However, swimming velocity approaching tens of times its body length per second remains a challenge for polymeric microrobots.

Miniaturized swimming robots have been conceptualized mostly with inorganic particle-based robots. Iron oxide microassemblies and nickel nanowires were previously proposed for tumbling motion on both flat or rough surfaces of water.<sup>[29–31]</sup> Recently, a slippery helical silica micropropeller with nickel deposition achieved propulsion in porcine vitreous with the viscosity of  $1.6 \text{ mPa s}$  ( $5 \text{ BL s}^{-1}$ ).<sup>[32]</sup> Janus microroller of silica and sputtered nickel demonstrated upstream locomotion in mouse whole blood.<sup>[33]</sup> In a swarming system, a submillimeter swarm of iron oxide nanoparticles was capable of swimming in various biofluids, including fetal bovine serum ( $1.1 \text{ mPa s}$ ), gastric acid ( $1.12 \text{ mPa s}$ ), blood plasma ( $1.9 \text{ mPa s}$ ), whole blood ( $4 \text{ mPa s}$ ), vitreous humor ( $150 \text{ mPa s}$ ), and hyaluronic acid ( $200 \text{ mPa s}$ ).<sup>[34]</sup> The rod-like, spring-like, and spherical inorganic robots could swim with translational motions following the rotations of the electromagnetic fields.

Previous studies on polymeric- and inorganic-based microrobots correlated swimming performances with either liquid viscosity or frequency of the rotating magnetic field. However, consideration for both variables is required for a full discussion of viscous drag in swimming microrobots. Hence, in this study, agile underwater orbital swimming of dense 3D polymeric microrobots ( $<56 \text{ BL s}^{-1}$ ) is scrutinized in viscosity-controlled solutions by experimental results and theoretical analysis. We have previously reported on the orbital maneuver of magnetic polymeric microrobots, namely, spinbots, that rotated and resultantly revolved by the rotation of two linearly connected permanent magnets.<sup>[8]</sup> Although the spinbots can locomote inside a liquid (Movie S1, Supporting Information), both the rotation and revolution behaviors are strongly affected by the viscous drag which can even result in motion failure. Thus, we investigate the critical conditions for rotational ability of spinbots in viscous media as well as deterministic orbital radius and velocity of the polymeric microrobots. Based on the analysis of their swimming behaviors, we demonstrate self-correcting orbital maneuver of spinbots on curvilinear and rough substrates filled with viscous solution having a viscosity of  $4.02 \text{ mPa s}$ , a model system for normal whole blood. Underwater orbital swimming can enable agile magnetic actuation, which is particularly desirable in robotics and biomedical applications.

## 2. Results and Discussion

### 2.1. Preparation and Actuation of Polymeric Microrobot

We prepared magnetically responsive 3D polymer nanocomposites composed of thermoplastic polyurethane (TPU) and iron oxide ( $\text{Fe}_3\text{O}_4$ ) nanoparticles ( $z$ -averaged diameter  $\approx 16 \text{ nm}$ ). The TPU– $\text{Fe}_3\text{O}_4$  nanocomposites were obtained using a rapid precipitation technique<sup>[35]</sup> for homogenous dispersion of magnetic particles in a polymer composite. In brief, the TPU and  $\text{Fe}_3\text{O}_4$  nanoparticles were mixed in a tetrahydrofuran (THF), a suitable mutual solvent, via ultrasonication. When the mixed solution was rapidly precipitated into methanol (MeOH), a poor mutual solvent, a rapid reduction in the polymer dimension produced nanoconfinement effects that prevented the phase separation of the  $\text{Fe}_3\text{O}_4$  nanoparticles from the TPU matrices (Figure 1a). The  $\text{Fe}_3\text{O}_4$  nanoparticles were dispersed in the TPU matrices at a 10 wt% concentration. The obtained TPU– $\text{Fe}_3\text{O}_4$  nanocomposite was mechanically compressed at an elevated temperature of  $175^\circ\text{C}$  with a  $70 \mu\text{m}$ -thick spacer and then cut into a  $20 \text{ mm}$  (length)  $\times$   $2 \text{ mm}$  (width) strip. To develop 3D helical architectures from the thin nanocomposite strip, we employed a torsion-induced shape-morphing method.<sup>[8]</sup> The high elongation and thermoplastic nature of the TPU facilitated large-strain twisting and stretching without permanent damage to the TPU– $\text{Fe}_3\text{O}_4$  nanocomposites. By repeating the  $180^\circ$  twisting process 30 times for the nanocomposite films, we effectively eliminated voids inside the 3D helical structure. To exclude undesirable supercoiling, the resultant architecture was lengthened to  $30 \text{ mm}$  and treated at an elevated temperature of  $175^\circ\text{C}$  for 20 min, followed by a quenching step. The optimized twisting conditions were designed to produce dense helical features (Figure 1b,c). Finally, dense 3D polymeric microrobots were created by cutting the helical architecture, which resulted in a body diameter of  $370 \mu\text{m}$ , body length of  $640 \mu\text{m}$ , and mass of  $0.18 \text{ mg}$ . The body length was fixed to be  $640 \mu\text{m}$  to elucidate the correlation between the magnetic propulsion and viscous drag on swimming spinbots in various viscous solutions.

Viscosity-controlled solutions were prepared by varying the glycerol concentration in water and actuated the spinbot at  $25^\circ\text{C}$ . The viscosities of the glycerol solutions at  $25^\circ\text{C}$  (Figure S1, Supporting Information) were calculated based on a previous study,<sup>[36]</sup> which reported the viscosity of water–glycerol solutions depending on temperature and glycerol concentration. While submerged in the viscous medium, the spinbot was actuated by rotating two linearly connected permanent magnets ( $<30 \text{ mT}$ ) with a single rotational axis underneath the container (Figure 1d). As the magnets rotated in clockwise (CW) direction, the spinbot rotated in the same direction with the same rotation frequency. The rotation frequency could be synchronized owing to the dense helical feature of the polymeric microrobot. Presence of voids in the microrobots resulted in a halt of the rotational movement.<sup>[8]</sup> During CW rotation, the spinbot also exhibited pivoting behavior (Figure 1e). In a static state of the magnetic field, one end of the lightweight robot was lifted along the direction of the out-of-plane magnetic field because the net magnetic moment of the spinbot aligns with it<sup>[37]</sup> (Figure S2, Supporting Information). The rotating magnetic field

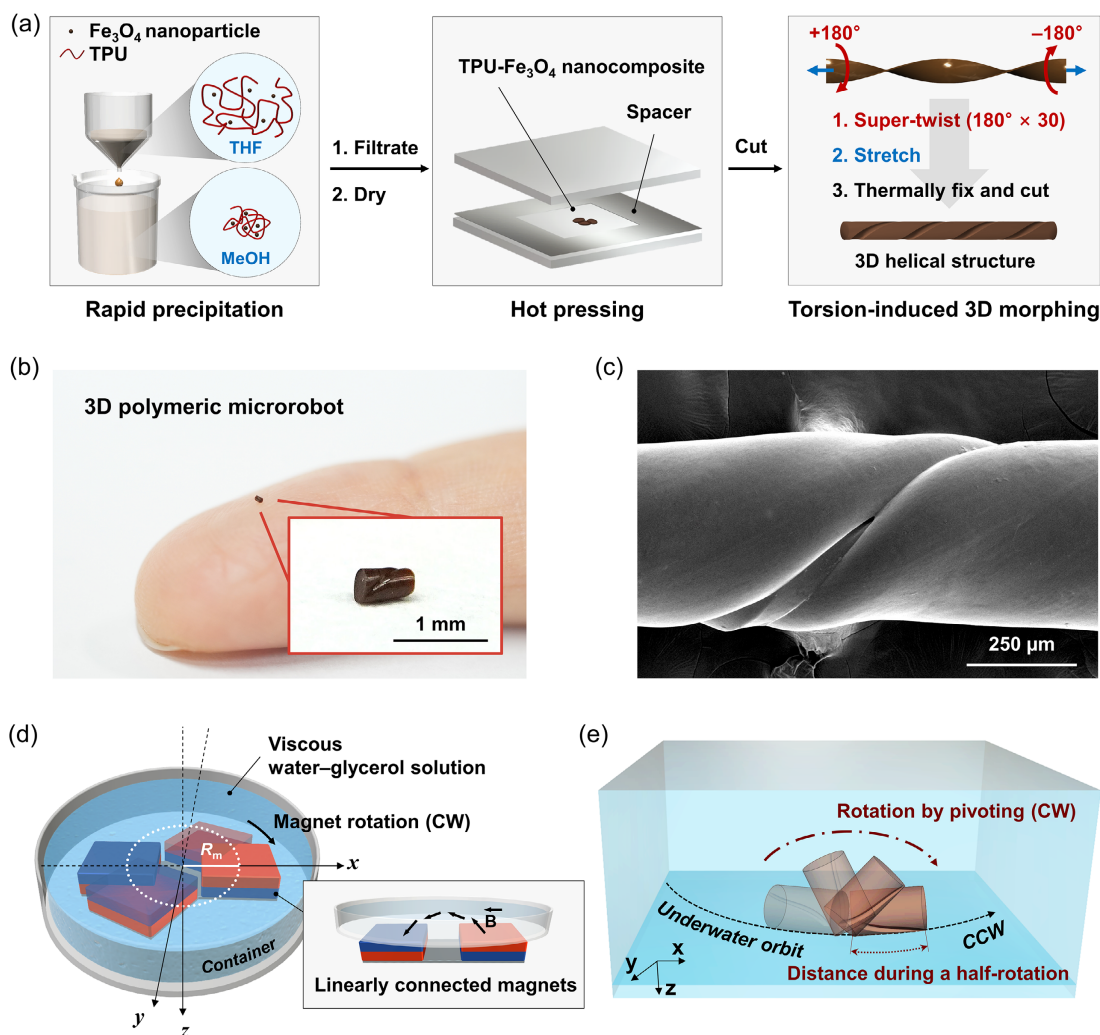


**Figure 1.** Miniaturized magnetic 3D polymeric microrobots for underwater orbital maneuver. a) Schematics of magnetic 3D polymeric microrobot preparation. b) Digital image of miniaturized polymeric microrobot with dense helical feature. c) Helical geometry confirmed by scanning electron microscope (SEM). d) Schematics of CW rotating permanent magnets underneath the solution container. The center-to-center distance of rotating magnetic axis and each magnet,  $R_m$ , is 24 mm. e) Schematics of underwater orbital swimming of spinbot. Counterclockwise (CCW) revolution is induced by CW rotational motility of the spinbot.

generates magnetic centripetal torque in the direction from the center of orbit toward the spinbot, enabling the pivoting motion. The revolution of the spinbot, as a result of the hierarchical swimming, forms an orbital radius within the center-to-center distance between the two magnets,  $R_m$ , which was 24 mm in our tested system.

## 2.2. Uniform Underwater Rotation

The pivoting spinbot continuously switched the contact points between the two end points of the robot body with the substrate in deionized water, as we rotated the magnets underneath the robot body at a frequency of 6.7 Hz (Figure 2a). At an increased magnetic frequency of 20 Hz, the spinbot exhibited tumbling motion with a jump; it instantly rotated without any contact with the substrate (Figure 2b, S3, and Movie S2, Supporting Information). Pivoting motion has

one to two contact points with the substrate, which is distinct from the tumbling motion with zero to one contact point. The underwater rotation of the spinbot enables revolution in the CCW direction; such pivoting or tumbling is possible only when the interfacial friction at the contact point is sufficient. For the swimming spinbot to pivot, the spinbot requires first to rotate with a uniform angular velocity in the solution, and this capability is strongly dependent on the liquid viscosity. The rotational ability of spinbots is achieved only when the magnitude of the magnetic rotational torque,  $T_{m,rot}$ , of the spinbot is larger than its viscous torque,  $T_{v,rot}$  ( $|T_{v,rot}| < |T_{m,rot}|$ ). For the theoretical calculation of the viscous torque and the magnetic rotational torque, we simplified the geometry of the spinbot to a horizontally laid cylinder and considered underwater swimming at low Reynolds numbers.<sup>[38,39]</sup> In a steady state, the viscous torque of the rotating spinbot inside a fluid can be estimated as

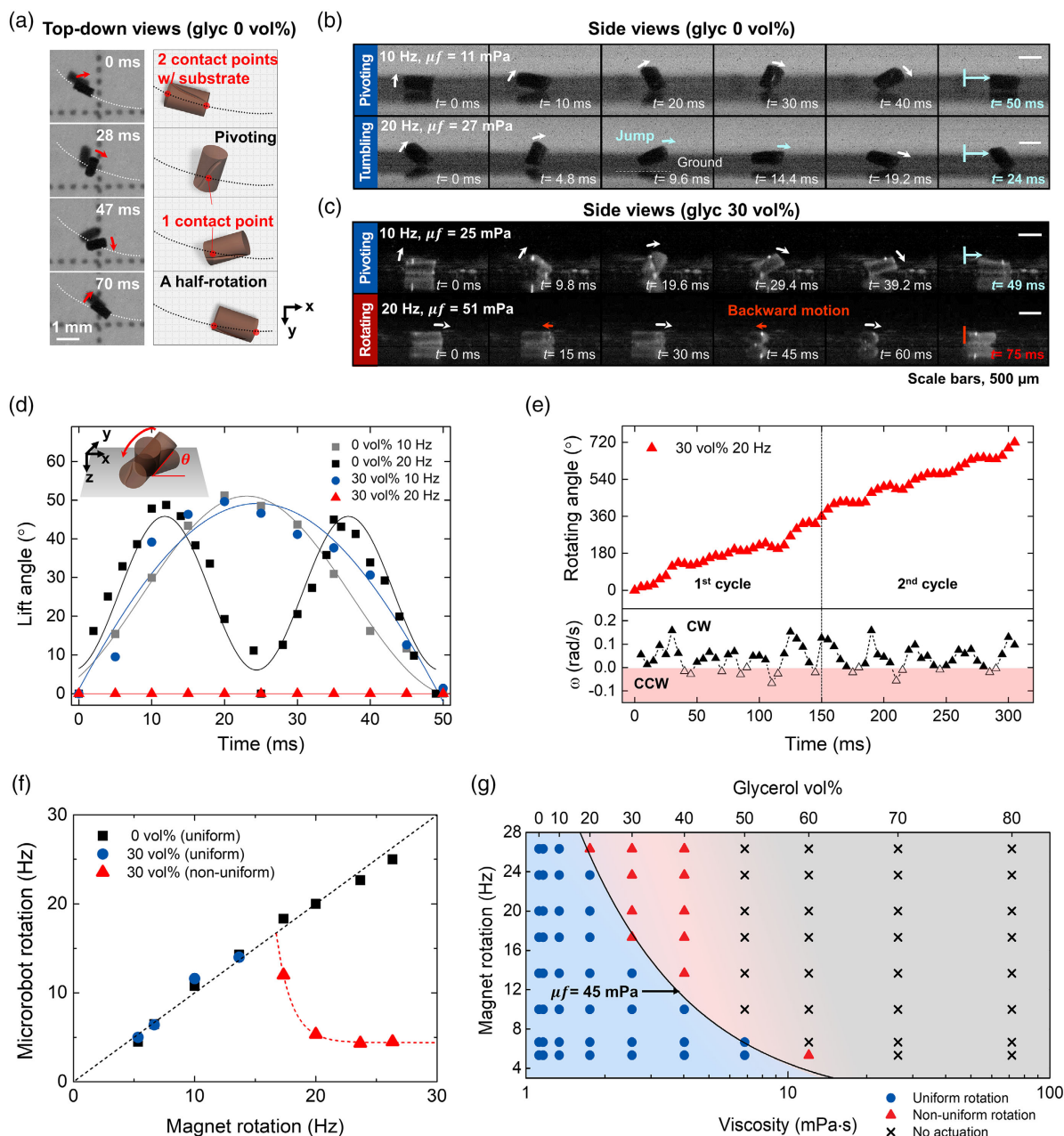


**Figure 2.** Underwater rotation in viscous solution. a) Pivoting motion of spinbot in water at a magnetic frequency of 6.7 Hz, confirmed by top-down view of slow motion and corresponding schematics. b, c) Effects of viscosity and frequency of magnet rotation by observation of half-rotation cycle of spinbot in b) water and c) glycerol–water solutions. d) Lift angle in the rotation of spinbots. e) Rotating angle in the nonuniform rotation at 2.5 mPa s of viscosity (30 vol% glycerol) and 20 Hz of magnet rotation. f) Frequency measurement of polymeric microbot rotation in the 30 vol% glycerol solution to confirm uniform and nonuniform regions. g) Diagram for rotational capability of spinbots depending on glycerol vol% in water at 25 °C.

$$|\mathbf{T}_{v,rot}| = \frac{\mu f}{2} \left( \frac{1}{2} + AR \right) d^3 T_v^* \quad (1)$$

where  $\mu$  is the liquid viscosity,  $f$  is the frequency of magnet rotation,  $AR$  and  $d$  are the aspect ratio and diameter of the spinbot

cross section, respectively, and  $T_v^*$  is the nondimensionalized torque. As shown in Equation (1), the viscous torque of the rotating spinbot is proportional to the frequency of the magnet rotation and the liquid viscosity. Ye et al. investigated the local flows around rotating microrobots inside a viscous medium via numerical simulations and showed that the viscous torque<sup>[39]</sup> of a horizontally laid cylinder,  $T_v^*$ , can be expressed as

$$T_v^* = 0.3769AR^{1.424} + 1.772. \quad (2)$$

The magnetic rotational torque by the time-varying magnetic field,  $\mathbf{T}_{m,rot}$ , can be in general represented as<sup>[21,22]</sup>

$$\mathbf{T}_{m,rot} = V(\mathbf{M}_{net} \times \mathbf{B}) \quad (3)$$

where  $V$  is the volume of the spinbot,  $\mathbf{M}_{net}$  is the net magnetic moment of the spinbot, and  $\mathbf{B}$  is the external magnetic field. In the case of spinbot rotation,  $\mathbf{T}_{m,rot}$  is generated by the directional mismatch between magnetic dipole moments inside the robot and the external magnetic field during magnetic relaxation when the spinbot becomes magnetized by the magnetic field. Therefore, Equation (3) can be expressed as

$$|\mathbf{T}_{m,rot}| = V|\mathbf{M}_{net}||\mathbf{B}| \sin(2\pi f t_{rel}) \quad (4)$$

where  $f$  is the frequency of magnet rotation and  $t_{rel}$  is the magnetic relaxation time. To identify the criterion for overcoming the viscous torque, magnetic torque needs to exceed viscous torque. In other words, the spinbot fails to rotate when the maximum magnetic torque is less than the viscous torque. The net magnetic moment of the spinbot is maximized when the magnitude of the external magnetic field is the greatest. Therefore, the criterion for the spinbot to rotate can be given as

$$|\mathbf{T}_{v,rot}| < |\mathbf{T}_{m,rot}|_{max} = V|\mathbf{M}_{net}|_{max}|\mathbf{B}|_{max}. \quad (5)$$

And from Equation (1) and (5), the criterion can be expressed as

$$\mu f < \frac{\pi|\mathbf{M}_{net}|_{max}|\mathbf{B}|_{max}}{2T_v^*} \left( \frac{1}{2AR} + 1 \right)^{-1} \quad (6)$$

Equation (6) shows that the rotational ability of spinbots depends on whether the product of the solution viscosity and frequency of magnet rotation, i.e.,  $\mu f$ , is greater or less than a critical value. If either the solution viscosity or the magnetic frequency increases, the viscous drag also increases; this increases the resistance against the motion of the spinbot, and the spinbot eventually fails to rotate when  $\mu f$  exceeds the critical value of 45 mPa for the AR-2 spinbot.

We experimentally verified that nonuniform rotation of the polymeric microrobot occurs when  $\mu f$  exceeds a critical value of 45 mPa (Figure 2b,c, Movie S3, Supporting Information). Within the critical value, the speed of magnet rotation corresponds to the number of rotations of the spinbot. Therefore, as shown in Figure 2b, the time required for the spinbot to rotate a half-cycle is reduced by half when the frequency of magnet rotation is doubled from 10 to 20 Hz in water with a viscosity of 1.12 mPa s. Pivoting and tumbling speed over the course of one rotation are measured to be 18.6 and 40.7 BL s<sup>-1</sup>, respectively (Figure S4, Supporting Information). Uniform underwater rotation implies that the spinbot can rotate stably with symmetrical variations in the lift angle (Figure 2d). Conversely, when  $\mu f$  exceeds the critical value of 45 mPa, the spinbot cannot rotate uniformly. As shown in Figure 2c, at 20 Hz and 30 vol% glycerol solution, the spinbot mainly rotates in the CW direction without a lift angle but repeatedly ceases rotation and occasionally rotates in the opposite direction. Due to the nonuniform actuation, the

polymeric microrobot (at 51 mPa) requires  $\approx 75$  ms to complete a half-cycle of rotation, which is three times the duration in pure water. The angular velocity,  $\omega$ , of the nonuniformly rotating spinbot fluctuates periodically with asymmetrical variation (Figure 2e). Considering that positive and negative angular velocities indicate CW and CCW rotation, respectively, the average interval between the CW and CCW rotations is calculated to be  $28 \pm 7$  ms. We experimentally scrutinized the number of rotations of the spinbot with respect to that of the permanent magnets (Figure 2f). In the 30 vol% glycerol solution, the spinbot had a rotational frequency corresponding to a magnet rotation of up to 13.7 Hz. The discrepancy appeared from a magnetic frequency of 17.3 Hz. The asynchronous rotation of the spinbot was predicted to occur beyond a critical frequency of 16.7 Hz, which is defined as the step-out frequency of a magnetic microrobot.<sup>[32,40,41]</sup> Figure 2g summarizes the conditions associated with various viscosities and frequencies of magnet rotation, which allow uniform underwater rotation of the spinbots. The maximum viscosity at which the spinbot can rotate uniformly is 6.84 mPa s, which corresponds to a 50 vol% glycerol solution.

### 2.3. Underwater Orbital Maneuvers

When the spinbot overcomes the viscous drag and rotates uniformly, it can pivot or tumble along an orbit (Figure S5, Supporting Information). The orbital behavior of the spinbot depends on the combined effect of the magnetic propulsion and viscous drag (Figure S6, Movie S4, Supporting Information). We tracked the underwater pivoting spinbots to analyze the correlation between the orbital radius and velocity according to the solution viscosity and magnetic frequency (Figure 3a–c). When  $\mu f$  is relatively small ( $\approx 7$  mPa), the spinbot revolves with a relatively small radius of  $\approx 6.4$  mm. The spinbot revolves with a larger orbital radius of 11.5 and 13.5 mm as  $\mu f$  increases to 15 and 25 mPa, respectively. We also observed that the orbital velocity strongly depends on the frequency of magnet rotation. The spinbot orbits at velocities of 3.9, 10.1, and 14.7 mm s<sup>-1</sup> when the frequency of magnet rotation is 5.3, 10, and 13.7 Hz, respectively.

To understand the complex relationship among the underwater orbital behaviors, liquid viscosity, and frequency of magnet rotation, we derived a mathematical model for the spinbots. When the two linearly connected magnetic blocks rotate under the spinbot, the magnetic force applied to the revolving spinbot can be expressed as<sup>[21,22]</sup>

$$[F_c, F_t, F_z]^T = V(\mathbf{M}_{net} \cdot \nabla)\mathbf{B} \quad (7)$$

where  $F_c$  is the magnetic centripetal force,  $F_t$  is the magnetic tangential force, and  $F_z$  is the magnetic force in a direction perpendicular to the surface (Figure S7, Supporting Information). The external magnetic field generated by the connected magnetic blocks can be calculated on the basis of Biot–Savart law (Supporting Note 1, Figure S8–S12, Supporting Information).<sup>[42,43]</sup> As the surface current forms a magnetization flow at eight sidewalls of each magnetic block, the external magnetic field can be approximated as

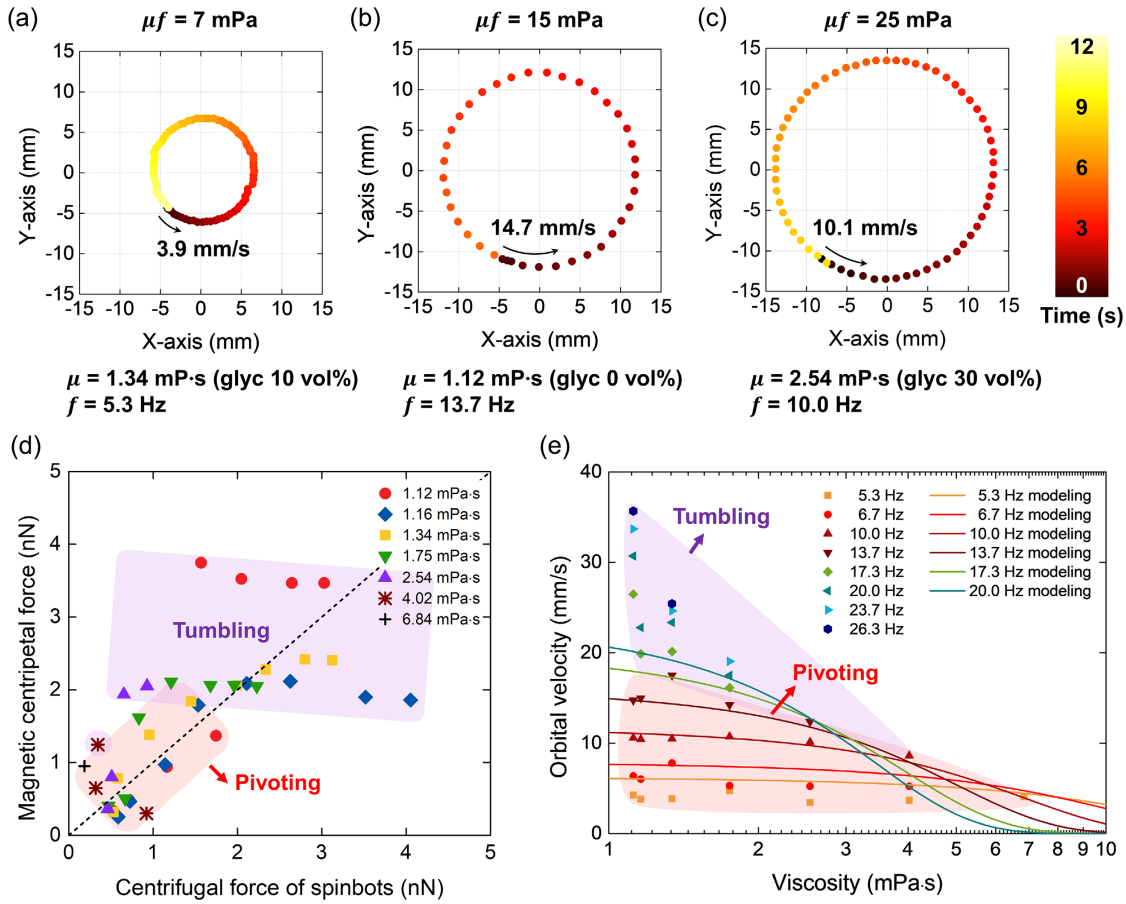


**Figure 3.** Orbit analysis of uniform actuation. a–d) Effect of  $\mu f$  on orbital radius of spinbot when the  $\mu f$  is a) 7 mPa, b) 15 mPa, and c) 25 mPa. d) Comparison of centrifugal force of the spinbot (experimental) and magnetic centripetal force (modeling) at a corresponding orbital radius, magnetic frequency, and liquid viscosity. e) Orbital velocity of the spinbot according to liquid viscosity at different frequencies of magnet rotation.

$$\mathbf{B}(R_{rv}, f, t) = \sum_{j=1}^{j=8} \mathbf{B}_j = \sum_{j=1}^{j=8} \int_{z=z_{\text{bottom}}}^{z=z_{\text{top}}} \int_{l=0}^{l=L} \frac{\mu_0 \mathbf{l}_j \times \mathbf{r}_j}{4\pi |\mathbf{r}_j|^3} \frac{I}{h} dl dz \quad (8)$$

where  $R_{rv}$  is the orbital radius of the spinbot,  $t$  is the rotation time of the magnetic blocks, and  $\mathbf{B}_j$  refers to the external magnetic field generated at  $j$ th surface of two magnetic blocks. The variable  $z_{\text{top}}$  and  $z_{\text{bottom}}$  are the  $z$ -axis coordinates of top and bottom side of the magnetic block, respectively, while  $L$  represents the length of the magnetic block and  $\mu_0$  is the vacuum permeability.  $\mathbf{l}_j$  is the unit vector of the fine-line conductor generated by finely dividing the sidewall,  $\mathbf{r}_j$  is the position vector from the fine-line conductor at  $j$ th surface to the spinbot,  $I$  is the equivalent surface current, and  $h$  is the height of magnetic block. The net magnetic moment of spinbot can be expressed as

$$\mathbf{M}_{\text{net}}(R_{rv}, f, t) = \alpha \mathbf{B}(R_{rv}, f, t - t_{\text{rel}}) \quad (9)$$

where  $\alpha$  is the constant of proportionality.

The magnetic force exerted upon the spinbot depends on the rotational frequency and the location of the spinbot. We performed further numerical analysis of the magnetic force based on Equation (7)–(9), which specifies that the frequency of magnet

rotation affects only the periodicity of the magnetic force while the magnitude remains constant (see Figure S10, Supporting Information). Therefore, the average amount of magnetic force is solely a function of the orbital radius, and its radial component,  $F_{c,\text{ave}}$ , can be derived as

$$\begin{aligned} |F_{c,\text{ave}}| = & -5.8137 \times 10^{-9} R_{rv}^6 + 1.0916 \times 10^{-6} R_{rv}^5 - 6.7624 \\ & \times 10^{-5} R_{rv}^4 + 1.3374 \times 10^{-3} R_{rv}^3 + 3.0757 \times 10^{-3} R_{rv}^2 \\ & - 8.0101 \times 10^{-3} R_{rv} \end{aligned} \quad (10)$$

where  $R_{rv}$  is the orbital radius. And for a revolving object, the centrifugal force,  $F_c$ , develops as

$$F_c = m \frac{v_{rv}^2}{R_{rv}} \quad (11)$$

where  $m$  is the mass of the spinbot and  $v_{rv}$  is its orbital velocity. While pivoting, the spinbot may find its equilibrium state, which involves a balance between magnetic centripetal and centrifugal forces. This balance is achieved by adjusting the orbital radius (Figure 3d). The orbital radius itself can be predicted with

Equation (10) and (11), once the dimension of the spinbot, liquid viscosity, and the frequency of the magnet rotation can be determined (see Figure S12, Supporting Information).

The orbital velocity of the spinbot is derived from the body length of the robot and its angular velocity only when the spinbot is able to pivot perfectly due to sufficient friction. However, the spinbot may slip inside the liquid when the viscous drag exceeds the interfacial friction. The slippage of the spinbot from the substrates occurs as the rotational inertial force exceeds the frictional force at the surface. We estimate the orbital velocity<sup>[8]</sup> of the spinbot considering the probability of slippage:

$$v_{rv} = \frac{l\omega_m}{\pi} (1 - \alpha_{\text{slip}}) = dARf \left[ 1 - \operatorname{erf} \left( \frac{2\pi\mu f d^2}{F_s} AR - 1 \right) \right] \quad (12)$$

where  $l$  is the body length of the spinbot,  $\omega_m$  is the angular velocity of magnets,  $\alpha_{\text{slip}}$  is the probability of slippage,  $F_s$  is the static friction force between the spinbot and the bottom plate (petri-dish), and  $\operatorname{erf}()$  is the error function to probability of slippage. As shown in Figure 3d,e, increasing the frequency of magnet rotation can lead to higher orbital velocity, thereby increasing the centrifugal force of the spinbot. According to Equation (12), the orbital velocity is considerably influenced by the frequency of magnet rotation, implying that orbital velocity increases at higher number of spinbot rotation.

When higher centrifugal force enlarges orbital radius, increased lift angle of spinbots induces a higher magnitude of magnetic centripetal torque (see Figure S2a and S9, Supporting Information). Both high magnetic centripetal torque and orbital velocity cause instantaneous jumping of the spinbot during pivoting, termed as tumbling. Due to the contact point to the substrate being between zero to one, the magnetic centripetal force deviates from the equalized centrifugal force of the tumbling spinbots at high frequencies of magnet rotation.

In Figure 3e, the orbital velocity of a tumbling spinbot exceeds the theoretical expectation, resulting in a maximum orbital velocity of  $35.7 \text{ mm s}^{-1}$  or a normalized velocity of  $56 \text{ BL s}^{-1}$  in water ( $1.12 \text{ mPa s}$ ,  $26.3 \text{ Hz}$ ,  $\mu f = 30 \text{ mPa}$ ). As the orbital velocity depends highly on the frequency of magnet rotation, we quantify energy conversion efficiency,  $mv_{rv}^2 / (2|T_{v,\text{rot}}|)$  (kinetic energy per viscous torque), and swimming performance output,  $v_{rv}/V$  (orbital velocity per robot volume) in Figure S13, Supporting Information.<sup>[44]</sup> Tumbling spinbot at  $26.3 \text{ Hz}$  ( $\mu f = 30 \text{ mPa}$ ) exhibits 2.4-fold higher energy conversion efficiency and 3.0-fold higher swimming performance output than pivoting spinbot at  $13.7 \text{ Hz}$  ( $\mu f = 15 \text{ mPa}$ ). Meanwhile, under identical conditions of magnetic frequency, an increase in the solution viscosity reduces the orbital velocity due to the increased probability of slippage. The orbital velocity of tumbling spinbot is measured to be  $25.4 \text{ mm s}^{-1}$  ( $40 \text{ BL s}^{-1}$ ) in a 10 vol% glycerol–water solution ( $1.34 \text{ mPa s}$ ,  $26.3 \text{ Hz}$ ,  $\mu f = 35 \text{ mPa}$ ). The spinbot exhibits swimmability in a 40 vol% glycerol–water solution at  $25^\circ \text{C}$  with a viscosity of  $4.02 \text{ mPa s}$ , which is regarded as the viscosity of normal whole blood at a physiological body temperature of  $36.5^\circ \text{C}$ .<sup>[45]</sup> At  $4.02 \text{ mPa s}$  and  $10 \text{ Hz}$ , the orbital velocity was measured to be  $5.5 \text{ mm s}^{-1}$  ( $8.5 \text{ BL s}^{-1}$ ). The spinbot is capable of swimming in solutions with a viscosity of up to  $6.84 \text{ mPa s}$  and exhibits an orbital velocity of up to  $4.1 \text{ mm s}^{-1}$  ( $6.4 \text{ BL s}^{-1}$ ) at  $5.4 \text{ Hz}$ .

## 2.4. Swimmability in Vascular-Like Environments

We demonstrated underwater swimming and self-correcting behavior of spinbots in vascular-like environments through the in-plane rotation of magnets with a magnetic frequency of  $6.7 \text{ Hz}$  (Figure 4). Self-correcting orbital maneuver is to circumvent obstacles without  $z$ -axial control of magnetic fields. The maneuver is induced by the force balance between centrifugal force of the spinbot and magnetic centripetal force. As the force balance leads to deterministic orbital radii, underwater orbital swimming enables this self-correcting behavior in spinbots. To observe the swimming behavior of the spinbot, a transparent small tube was filled with a solution having a viscosity of  $4.02 \text{ mPa s}$  (Figure 4a). As the orbital maneuverability of the spinbot is provided by rotating two permanent magnets, linear translation of the magnets without rotation cannot actuate the spinbot (Figure 4b and Movie S5, Supporting Information). The spinbot is steered on-demand by slowly moving the position of the tube along the orbiting direction (Figure S14, Supporting Information). The positional movement of the tube indicates translation of the magnetic axis. The spinbot can swim long distances of  $195 \text{ BL}$  along the horizontal direction of the magnetic axis (Figure S15 and Movie S6, Supporting Information). As shown in the side view in Figure 4c, the high-speed and high-magnification observation of the spinbot confirmed underwater swimming at a curvilinear wall. Owing to the agile hierarchical locomotion involving rotation and resultant revolution, the polymeric microrobot could climb a coarse hill composed of granules with an average diameter of  $250 \mu\text{m}$  (Figure 4d and Movie S7, Supporting Information). The self-correcting underwater swimming could be manipulated simply through the horizontal axial movement of the magnets, without the need for  $z$ -axial control.

We validated the swimming capability of the spinbots at a rough inner wall of a commercial artificial blood vessel (Figure 4e). Artificial blood vessel structures are designed to be porous to ensure vascular permeability, as shown in Figure 4f–h and Figure S16, Supporting Information. Due to this porosity, the inner wall has rough surfaces with a root-mean-square roughness of  $3.5 \mu\text{m}$  and a maximum peak height of  $15.9 \mu\text{m}$ . Despite the possible interference from the rough surfaces with the actuation of the polymeric microrobot, as shown in Figure 4i, the pivoting spinbot could successfully swim forward in the artificial blood vessel filled with the viscous solution ( $4.02 \text{ mPa s}$ ). However, swimming performance is required to be implemented in vivo circulatory systems that are characterized by continuous and pulsatile blood flow. We expect that forward swimming for spinbots would be feasible in blood vessels with a diameter of  $4 \text{ mm}$  and with a flow velocity<sup>[27]</sup> of  $0.2 \text{ mm s}^{-1}$ , considering that an orbital velocity of  $5.5 \text{ mm s}^{-1}$  ( $8.5 \text{ BL s}^{-1}$ ) was achieved in the viscous solution with viscosity of  $4.02 \text{ mPa s}$ . Spinbot actuation in an artery requires further investigation as the blood flow velocity of an artery<sup>[46]</sup> can reach  $20 \text{ cm s}^{-1}$  and may hinder orbital swimming. To improve the swimming performance and velocity of spinbots, we plan to employ magnetic systems with a higher magnetic flux density and enhance the magnetic response of polymer composites.

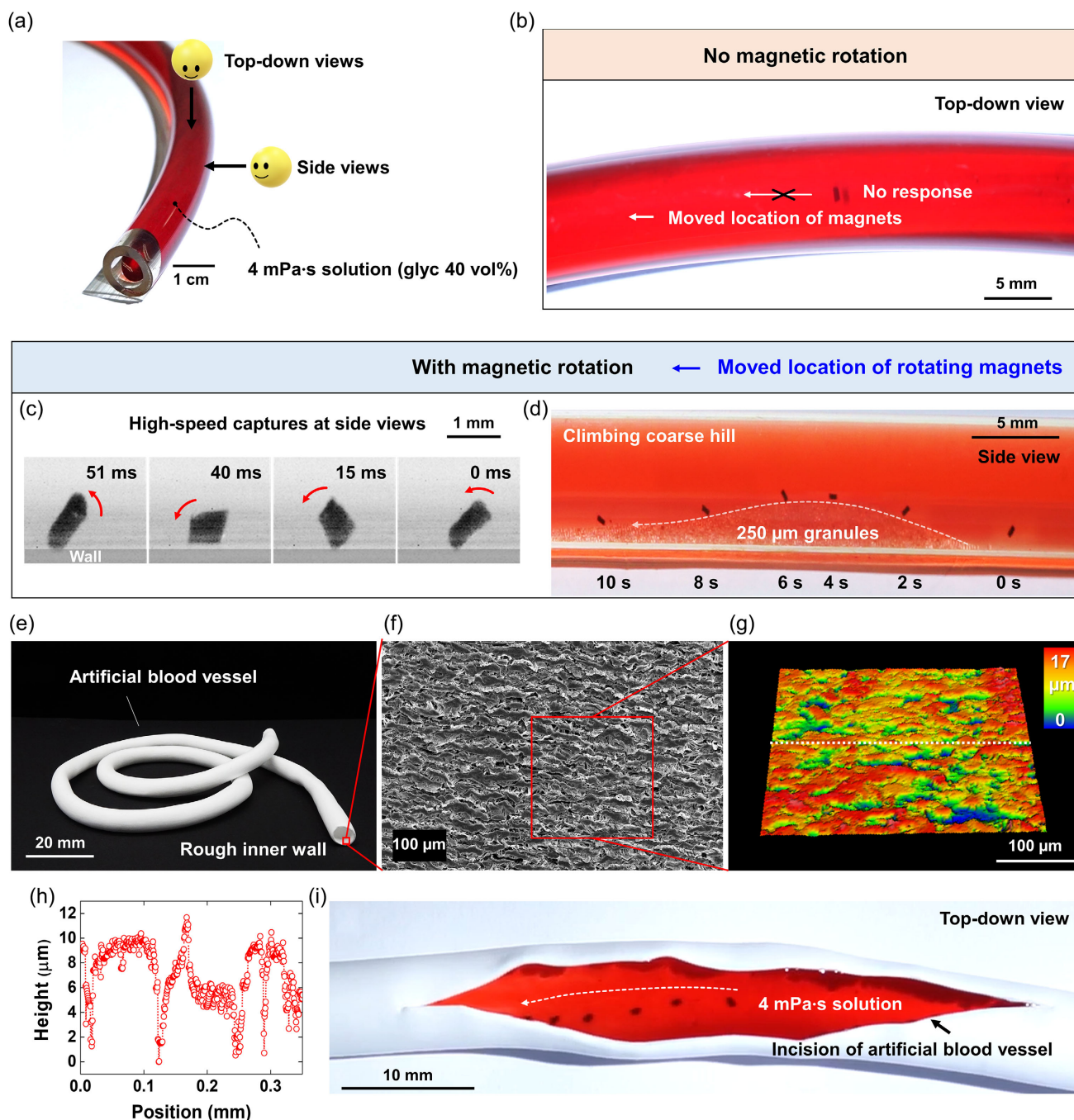


**Figure 4.** Underwater swimmability on curvilinear and rough substrates. a–d) Actuation in a tube where the wall thickness is 2 mm and inner diameter is 7 mm. a) Transparent tube filled with glycerol–water solution to confirm swimming behavior of spinbots. b) Spinbot incapable of swimming when location of magnets is moved without rotating. c) Underwater swimming of spinbot in the tube when the magnets underneath the substrate rotate. d) Spinbot climbing coarse hill consisting of granular particles with 250  $\mu\text{m}$  diameter. e–i) Actuation in an artificial blood vessel where the wall thickness is 750  $\mu\text{m}$  and inner diameter is 6 mm. e) Digital image of the artificial blood vessel. f–g) Rough inner surface confirmed by f) SEM micrograph and g) 3D optical profile. h) Height information from the 3D optical profile. i) Underwater orbital swimming of spinbot on the rough surface of artificial blood vessel for 10 s. The solutions in (a–i) have a viscosity of 4.02 mPa s, similar to whole normal blood.

### 3. Conclusions

The objective of our study is to demonstrate agile underwater swimming ability of the polymeric microrobots and investigate the correlation between magnetic propulsion and viscous drag in the viscous solutions for the microrobots. The results reveal that underwater swimming velocity can be improved by employing the spinbot processed with thermoplastic polymeric nanocomposites when compared to that of previous swimming polymeric microrobots. The 3D twisted helical polymer nanocomposite is prepared to impart agile swimmability via torsion-induced morphing of the 2D TPU–Fe<sub>3</sub>O<sub>4</sub> nanocomposite film. Owing to the dense 3D body without voids, underwater rotation of the spinbot is synchronized in response to rapidly rotating magnets up to the magnetic frequency of 26.3 Hz. However, in viscous media the spinbots can swim only when the applied magnetic rotational torque overcomes the viscous drag. Otherwise, the polymeric microrobot shows a nonuniform rotation or halt of actuation, and the criterion for rotational ability is determined by the product of fluid viscosity and frequency of magnet rotation.

Through theoretical modeling of underwater rotation and revolution, we confirm that the hierarchical locomotion of the spinbot is a hybrid-driven motion of magnetic centripetal torque and magnetic centripetal force caused by rotating permanent magnets. As magnetic centripetal torque is generated to the spinbot by the interaction between the lifted spinbot and the external field, the underwater rotation evolves into revolutions via pivoting or tumbling motions. The spinbot swims along the deterministic orbits continuously due to the force balance between the centrifugal force of spinbots and the centripetal force of magnets. While the orbital radius is determined by both the liquid viscosity and the frequency of magnet rotation via force balance, the change in orbital velocity is susceptible to the frequency of magnet rotation. The polymeric microrobot achieves underwater orbital velocity of up to 35.7 mm s<sup>-1</sup> at 26.3 Hz despite the small magnetic flux density (<30 mT).

The spinbot demonstrates forward swimming via orbital maneuvers in viscous solutions with viscosity comparable to or higher than that of normal whole blood (4 mPa s). The hierarchical locomotion provides self-correcting orbital swimmability that can circumvent obstacles without changing the magnetic frequencies. Hence, the spinbot can swim in vascular-like environments, although rotational motility of the spinbot is impeded to some extent by the coarse granular hills in the stenosed tube and/or the rough substrate in the artificial blood vessel. We envision that the spinbots facilitate navigation inside internal organs, such as wrinkled stomachs, tortuous intestines, and blood vessels by simply adjusting the position of the permanent magnets. Particularly, the spinbot shows great potential swimmability in rough endothelia of blood vessels as well as narrowed blood vessels by atherosclerotic plaque. Overall, this agile swimming motility based on orbital maneuvers offers a promising actuation strategy for practical applications in biomedical engineering, such as drug transportation, medical imaging, cell manipulation, and disease diagnosis.

### 4. Experimental Section

*Preparation of Polymeric Microrobots:* Dense helical polymeric microrobots were prepared using a previously reported method.<sup>[8]</sup> Thermoplastic

polyurethane (TPU) (KOLON Industries, ELLAS K-185 A) was dissolved in tetrahydrofuran (THF) (Fisher Scientific International, Inc., J. T. Baker) for 7 days. Iron oxide nanoparticles (Ferrotec Corporation, EMG1300, Fe<sub>3</sub>O<sub>4</sub>) were sonicated in THF for 1 h. The dispersed Fe<sub>3</sub>O<sub>4</sub> solution was mixed with the TPU solution, followed by sonication for 5 min. TPU–iron oxide (TPU–Fe<sub>3</sub>O<sub>4</sub>) nanocomposite with 10 wt% incorporation of the nanoparticles was obtained by rapid precipitation of the mixed solution of TPU and Fe<sub>3</sub>O<sub>4</sub> into methanol (Samchun Chemical Co., Ltd.). The solvents were filtered, and the residual solvents in the TPU–Fe<sub>3</sub>O<sub>4</sub> nanocomposite were dried in a vacuum oven at 40 °C for 7 days. A 70 μm-thick polymer nanocomposite film was prepared by hot-pressing at 175 °C for 8 min and then cut into strips of 20 mm × 2 mm. For the construction of the helical structure, both ends of the TPU pressing Fe<sub>3</sub>O<sub>4</sub> nanocomposite strip were twisted by 180° left-handed rotations. The torsion process was repeated 30 times, followed by stretching of the twisted strip to 30 mm. The 3D helix in the cylindrical shape of the TPU–Fe<sub>3</sub>O<sub>4</sub> nanocomposite was thermally fixed in a vacuum oven at 175 °C for 20 min. By cutting the 3D helical structures, a polymeric microrobot was prepared with a body length of 640 μm, which corresponded to an aspect ratio of 1.7 (AR-1.7).

*Characterization of Underwater Swimming in Viscous Solution:* Glycerol (Samchun Chemical Co., Ltd.) was vortex-mixed with deionized water at 2200 rpm for 1 min so that the concentration range of glycerol in the glycerol–water solution was from 0 vol% to 80 vol%. The polymeric microrobot was actuated in water, and the viscous solution was filled in a petri-dish container at 25 °C using a magnetic stirrer (Misung Scientific. Co. Ltd., HS180). The dimensions of each permanent magnet were 30 mm × 30 mm × 10 mm. The starting point of the polymeric microrobot was the substrate center of the magnetic stirrer. Underwater orbits of the polymeric microrobots were analyzed when speeds of the rotating magnets in the stirrer were varied to be 5.3, 6.7, 10.0, 13.7, 17.3, 20.0, 23.7, and 26.3 Hz. The rotational angle and frequency of the polymeric microrobots were analyzed using a high-speed camera (Vision Research, Phantom, Micro C110). The polymeric microrobot was placed in a transparent tube and an artificial blood vessel (WELCRON Co., Ltd., e-PTFE STRETCH) when the tubes were filled with a glycerol–water solution with 40 vol% concentration of glycerol. The red pigment was blended with the 40 vol% glycerol–water solution to distinguish the solution filled with the tubes. The wall roughness in the artificial blood vessel was measured using a 3D optical profiler (Zygo Corporation, NewView 7300).

### Supporting Information

Supporting Information is available from the Wiley Online Library or from the author.

### Acknowledgements

S.W. and H.J. contributed equally to this work. This work was supported by National Research Foundation of Korea (grant nos. NRF-2019R1A2C1004559 and NRF2019M3D1A2103919) and the KAIST Creative & Challenging Research Program (C2 Project). The authors appreciate Prof. Myeong-Woo Cho at Inha University for facilitating the use of the 3D optical profiler.

Note: The Supporting Information was amended on June 21, 2022, after initial publication online.

### Conflict of Interest

The authors declare no conflict of interest.

### Data Availability Statement

The data that support the findings of this study are available from the corresponding author upon reasonable request.

## Keywords

magnetic actuation, microrobots, polymer nanocomposites, underwater swimming, untethered miniaturized robots

Received: December 20, 2021

Revised: March 3, 2022

Published online: March 20, 2022

- [1] D. J. Preston, H. J. Jiang, V. Sanchez, P. Rothmund, J. Rawson, M. P. Nemitz, W.-K. Lee, Z. Suo, C. J. Walsh, G. M. Whitesides, *Sci. Robot.* **2019**, 4, eaaw5496.
- [2] A. Kotikian, C. McMahan, E. C. Davidson, J. M. Muhammad, R. D. Weeks, C. Daraio, J. A. Lewis, *Sci. Robot.* **2019**, 4, eaax7044.
- [3] J. K. Park, K. Nan, H. Luan, N. Zheng, S. Zhao, H. Zhang, X. Cheng, H. Wang, K. Li, T. Xie, Y. Huang, Y. Zhang, S. Kim, J. A. Rogers, *Adv. Mater.* **2019**, 31, 1905715.
- [4] J. J. Wie, M. R. Shankar, T. J. White, *Nat. Commun.* **2016**, 7, 13260.
- [5] Y.-C. Cheng, H.-C. Lu, X. Lee, H. Zeng, A. Priimagi, *Adv. Mater.* **2020**, 32, 1906233.
- [6] M. Pilz da Cunha, S. Ambergen, M. G. Debije, E. F. G. A. Homburg, J. M. J. den Toonder, A. P. H. J. Schenning, *Adv. Sci.* **2020**, 7, 1902842.
- [7] H. Shahsavan, A. Aghakhani, H. Zeng, Y. Guo, Z. S. Davidson, A. Priimagi, M. Sitti, *Proc. Natl. Acad. Sci. U. S. A.* **2020**, 117, 5125.
- [8] S. Won, S. Kim, J. E. Park, J. Jeon, J. J. Wie, *Nat. Commun.* **2019**, 10, 4751.
- [9] Y. Kim, G. A. Parada, S. Liu, X. Zhao, *Sci. Robot.* **2019**, 4, eaax7329.
- [10] Z. Ren, W. Hu, X. Dong, M. Sitti, *Nat. Commun.* **2019**, 10, 2703.
- [11] J. G. Kim, J. E. Park, S. Won, J. Jeon, J. J. Wie, *Materials* **2019**, 12, 3065.
- [12] W. Cho, J. Jeon, W. Eom, J. G. Lee, D. Kim, Y. S. Kim, T. H. Han, J. J. Wie, *Adv. Funct. Mater.* **2021**, 31, 2102106.
- [13] J. G. Kim, J. Jeon, R. Sivakumar, J. Lee, Y. H. Kim, M. Cho, J. H. Youk, J. J. Wie, *Adv. Intell. Syst.* **2021**, 3, 2100148.
- [14] Y. Zhao, C. Xuan, X. Qian, Y. Alsaïd, M. Hua, L. Jin, X. He, *Sci. Robot.* **2019**, 4, eaax7112.
- [15] J. Jeon, J.-C. Choi, H. Lee, W. Cho, K. Lee, J. G. Kim, J.-W. Lee, K.-I. Joo, M. Cho, H.-R. Kim, J. J. Wie, *Mater. Today* **2021**, 49, 97.
- [16] M. Dong, X. Wang, X.-Z. Chen, F. Mushtaq, S. Deng, C. Zhu, H. Torlakcik, A. Terzopoulou, X.-H. Qin, X. Xiao, J. Puigmartí-Luis, H. Choi, A. P. Pêgo, Q.-D. Shen, B. J. Nelson, S. Pané, *Adv. Funct. Mater.* **2020**, 30, 1910323.
- [17] Y. Dai, S. Liang, Y. Chen, Y. Feng, D. Chen, B. Song, X. Bai, D. Zhang, L. Feng, F. Arai, *Adv. Intell. Syst.* **2020**, 2, 1900148.
- [18] J. Li, X. Li, T. Luo, R. Wang, C. Liu, S. Chen, D. Li, J. Yue, S. Cheng, D. Sun, *Sci. Robot.* **2018**, 3, eaat8829.
- [19] C. Li, G. C. Lau, H. Yuan, A. Aggarwal, V. L. Dominguez, S. Liu, H. Sai, L. C. Palmer, N. A. Sather, T. J. Pearson, D. E. Freedman, P. K. Amiri, M. O. de la Cruz, S. I. Stupp, *Sci. Robot.* **2020**, 5, eabb9822.
- [20] H. Gu, Q. Boehler, H. Cui, E. Secchi, G. Savorana, C. De Marco, S. Gervasoni, Q. Peyron, T. Y. Huang, S. Pane, A. M. Hirt, D. Ahmed, B. J. Nelson, *Nat. Commun.* **2020**, 11, 2637.
- [21] W. Hu, G. Z. Lum, M. Mastrangeli, M. Sitti, *Nature* **2018**, 554, 81.
- [22] G. Z. Lum, Z. Ye, X. Dong, H. Marvi, O. Erin, W. Hu, M. Sitti, *Proc. Natl. Acad. Sci. U. S. A.* **2016**, 113, E6007.
- [23] I. C. Yasa, H. Ceylan, U. Bozuyuk, A. M. Wild, M. Sitti, *Sci. Robot.* **2020**, 5, eaaz3867.
- [24] X. Wang, X.-H. Qin, C. Hu, A. Terzopoulou, X.-Z. Chen, T.-Y. Huang, K. Maniura-Weber, S. Pané, B. J. Nelson, *Adv. Funct. Mater.* **2018**, 28, 1804107.
- [25] H. W. Huang, F. E. Uslu, P. Katsamba, E. Lauga, M. S. Sakar, B. J. Nelson, *Sci. Adv.* **2019**, 5, eaau1532.
- [26] X. Wang, C. Hu, S. Pane, B. J. Nelson, *IEEE Robot. Autom. Lett.* **2021**, 7, 1682.
- [27] H. Xu, M. Medina-Sánchez, M. F. Maitz, C. Werner, O. G. Schmidt, *ACS Nano* **2020**, 14, 2982.
- [28] A. Aziz, S. Pane, V. Iacovacci, N. Koukourakis, J. Czarske, A. Mencias, M. Medina-Sánchez, O. G. Schmidt, *ACS Nano* **2020**, 14, 10865.
- [29] C. E. Sing, L. Schmid, M. F. Schneider, T. Franke, A. Alexander-Katza, *Proc. Natl. Acad. Sci. U. S. A.* **2010**, 107, 535.
- [30] L. Zhang, T. Petit, Y. Lu, B. E. Kratochvil, K. E. Peyer, R. Pei, J. Lou, B. J. Nelson, *ACS Nano* **2010**, 4, 6228.
- [31] T. Petit, L. Zhang, K. E. Peyer, B. E. Kratochvil, B. J. Nelson, *Nano Lett.* **2012**, 12, 156.
- [32] Z. Wu, J. Troll, H. H. Jeong, Q. Wei, M. Stang, F. Ziemssen, Z. Wang, M. Dong, S. Schnichels, T. Qiu, P. Fischer, *Sci. Adv.* **2018**, 4, eaat4388.
- [33] Y. Alapan, U. Bozuyuk, P. Erkoc, A. C. Karacakol, M. Sitti, *Sci. Robot.* **2020**, 5, eaba5726.
- [34] J. Yu, D. Jin, K. F. Chan, Q. Wang, K. Yuan, L. Zhang, *Nat. Commun.* **2019**, 10, 5631.
- [35] M. E. Mackay, A. Tuteja, P. M. Duxbury, C. J. Hawker, B. Van Horn, Z. Guan, G. Chem, R. S. Krishnan, *Science* **2006**, 311, 1740.
- [36] J. M. Kim, F. Wolf, S. K. Baier, *Tribol. Int.* **2015**, 89, 46.
- [37] E. Diller, J. Giltinan, G. Z. Lum, Z. Ye, M. Sitti, *Int. J. Rob. Res.* **2016**, 35, 114.
- [38] Q. Liu, A. Prosperetti, *J. Fluid Mech.* **2010**, 657, 1.
- [39] Z. Ye, A. Jana, M. Sitti, arXiv Prepr. **2020**, arXiv2003.05908.
- [40] A. W. Mahoney, N. D. Nelson, K. E. Peyer, B. J. Nelson, J. J. Abbott, *Appl. Phys. Lett.* **2014**, 104, 144101.
- [41] A. Spatafora-Salazar, D. M. Lobmeyer, L. H. P. Cunha, K. Joshi, S. L. Biswal, *Soft Matter* **2021**, 17, 1120.
- [42] E. P. Furlani, *Permanent Magnet and Electromechanical Devices: Materials, Analysis, and Applications*, Academic Press, Cambridge, MA **2001**.
- [43] R. Ravaud, G. Lemarquand, V. Lemarquand, C. Depollier, *IEEE Trans. Magn.* **2008**, 44, 1982.
- [44] A. Pena-Francesch, J. Giltinan, M. Sitti, *Nat. Commun.* **2019**, 10, 3188.
- [45] L. Liu, D. Hu, R. H. W. Lam, *Micromachines* **2020**, 11, 934.
- [46] M. Klarhöfer, B. Csapo, C. Balassy, J. C. Szeles, E. Moser, *Magn. Reson. Med.* **2001**, 45, 716.